Strong Host–Guest Dependence on the Emissive Properties of MOF-5 and [Zn 2 (BTTB)(DMF) 2 •(H 2 O) 3] n

Adrien Schlachter, Paul Asselin, Daniel Fortin, Paul-Ludovic Karsenti, Pierre Harvey

Strong host-guest dependence on the emission properties of MOF-5 and $[Zn_2(BTTB)(DMF)_2 \bullet (H_2O)_3]_n$

Adrien Schlachter,[1] Paul Asselin,[1] Daniel Fortin,[1] Paul-Ludovic Karsenti[1] and Pierre D. Harvey[1]*

1- Département de Chimie, Université de Sherbrooke, 2500 Boul. de l'Université, Sherbrooke (QC), J1K 2R1

Abstract. 3D-$[Zn_4O(1,4\text{-BDC})_3 \bullet x(\text{solvent})]_n$ (**MOF-5**; BDC = 1,4-benzodicarboxylate), and 3D-$[Zn_2(BTTB)(DMF)_2 \bullet (H_2O)_3]_n$ (**MOF-D**; BTTB = 4,4′,4″,4‴-benzene-1,2,4,5-tetrayltetrabenzoate), have been investigated by means of steady state UV-visible and fluorescence and time-resolved emission spectroscopy, as a function of solvent and power of the excitation irradiation. The low-temperature X-ray structures (173 K) permitted to locate solvent molecules (here H_2O) in the lattice. They were found distributed in the middle in the voids with no evidence for interactions (H-bond, coulombic, dipole-dipole). The fluorescence decays of the ligands (ππ* excited state), τ_F, for the host guest composite **MOF-5**@solvent and **MOF-D**@solvent (solvent = air, MeCN, EtCN, MeOH, EtOH, DMF) were found bi-exponential (short τ_{F1} (ps), and long τ_{F2} (ns)) with one important feature: upon cooling from 298K to 77K, τ_{F1} (ps) and τ_{F2} (ns), decreases and increases, respectively. The low values for τ_{F1} (ps) is associated with the augmented probability of solvent-ligand collisions leading to non-radiative deactivation, which upon cooling to 77K increases further as the scaffolding contracts. The augmentation in τ_F (τ_{F2}) is readily associated with the increase rigidity of the ligands that are not submitted to this effect (at the surface of the MOF and as pendent groups). Upon increasing the excitation flux, the fluorescence intensity increases linearly with the laser power indicating absence of singlet-singlet annihilation, thus absence of efficient exciton migration. This observation is explained by the small absorptivity coefficients, which leads to small ***J*** spectral overlap between absorption and fluorescence according to the Forster and Dexter theories, and consequently, small rate for energy migration. This conclusion drastically changes the perception of the photocatalytic mechanism of **MOF-5** and other MOFs exhibiting similar absorption features (i.e. no antenna effect).

Introduction

Metal-Organic Frameworks (MOFs) are known to exhibit rich heterogeneous excited-state driven catalytic activity[1] and the semiconducting and emissive **MOF-5** (3D-$[Zn_4O(1,4\text{-}BDC)_3]_n$) (BDC = 1,4-benzodicarboxylate) has been found to make no exception over the past several years. Indeed, semiconductor@**MOF-5** composites have become notorious for various photocatalytic applications such as H_2-production,[2–9] O_2-evolution,[10] degradation of toxic organics and pollutants,[11–20] bacterial inactivation,[21–23] Cr(VI)-reduction[24] and organic reactions.[25] **MOF-5** is also known to be fluorescent, and this property has been used to design various emission-based sensors for toxic chemicals such as cationic heavy metal(II)[26,27] and pesticides.[28] The nature of the fluorescent state has been the subject of debate, but was recently established to be ligand-centered with the particularity that major photophysical parameters, such as band shape, band position (in the 325-500 nm window) and fluorescence decays are strongly guest-dependent (air, DMF, water-content).[29] An earlier explanation was ligand-to-ligand charge transfer, LLCT, which was supported by the high structural sensitivity of **MOF-5** towards water,[30] and by a theoretical study.[31] In the former investigation, a long exposure (days) provokes metal-ligand bond breaking, framework dislocation and a blue-shift of the fluorescence band.[30] The high sensitivity of **MOF-5**'s fluorescence properties (*i.e.* band shape and band maximum) towards organic guest molecules, such as DMF, ethanol, o- m- and p-xylene, for example, was also reported in another study.[32] Occasionally, a red-shifted emission band (λ_{max} ~514-518 nm) was also recorded and was assigned to cluster-centered Zn_4O, (*i.e.* quantum dot-like)[33] and ligand-centered phosphorescence.[34] However, it appears that small amounts of ZnO nanoparticles (NPs) as impurites inside **MOF-5** give the exact same broad luminescence signal associated with neat ZnO NPs.[35,36]

Similarly to 1,4-BDC, the ligand 4,4′,4″,4‴-benzene-1,2,4,5-tetrayltetrabenzoate (BTTB) is known to form various MOFs. Two of them exhibit weak BTTB-centered fluorescence in the solid state (3D-$[Zn_2(BTTB)\bullet(H_2O)_5]_n$; λ_{max} ~ 470 nm)[37] and suspended in DMF (3D-$[Zn_2(BTTB)(bpeb)\bullet(bped)\bullet 4H_2O]_n$, bpeb = 1,4-bis(2-(4-pyridyl)ethenyl)benzene, λ_{max} ~ 470 nm when the vibronically structured bpeb fluorescence is completely quenched),[38] have been collected. Contrary to **MOF-5** and to the best of our knowledge,

no investigation of BTTB-containing MOFs focusing on the variation of their fluorescence properties as a function of guest molecules, has been reported.

The efficiency of heterogeneous photocatalysis depends, among several parameters, on the efficiency (*i.e.* rate and distance) of exciton migration through the framework,[39–42] which depends on the framework structure.[43,44] We now report the power dependence of the fluorescence intensity and lifetimes of 3D-$[Zn_2(BTTB)(DMF)_2 \bullet (H_2O)_3]_n$[45] hereafter designated **MOF-D** (for which no photophysical properties have been reported so far) and **MOF-5** as a function of solvent molecules inside the pores (guests). It is found that in both cases, these parameters are strongly dependent on the nature of the guest molecule.

Experimental Section

Materials. **Reagents:** Common solvents, zinc nitrate hexahydrate (reagent grade, 98%), terephthalic acid (98%), and N,N'-dimethylformamide (ACS reagent ≥ 99.8%) were purchased from Millipore Sigma or Oakwood Chemical. Reagents were used without further purification. Solvents were either used as-is, or distilled over desiccants under inert atmosphere. DMF for MOF syntheses was dried over 4 Å molecular sieves.

MOF-5 was prepared from a modified procedure of the literature.[46,47] Terephtalic acid (44 mg, 0.27 mmol) was added to a 50 mL glass vial with DMF (25 mL). The vial was sonicated until all material dissolved. Zinc nitrate hexahydrate (229 mg, 0.77 mmol) was then added, and the vial was capped. The mixture was gently swirled until the solution becomes crystal clear. The closed vial was then placed in an oven preheated to 80°C for 10 hours. The vial was removed from the oven to cool down to room temperature. Clear crystals of **MOF-5** adhering to the vial walls were collected and washed with fresh DMF. $[Zn_2(BTTB)(DMF)_2 \bullet (H_2O)_3]_n$ was prepared according to procedure outlined in the literature.[45]

MOF activation: Both MOFs were activated in a vacuum oven at 120 °C for at least 8h and kept in sealed vials in a desiccator. Small batches were reactivated as required. Structures and phase homogeneity were confirmed by single crystal and powder X-ray crystallography.

Solvent molecules insertion: Following activation, small batches of both MOF were placed inside small vials, which were placed, uncapped in larger vials containing a small

amount of DMF, EtOH, MeOH, EtCN, or MeCN. The larger vial was sealed and left untouched for several days to allow vapour diffusion. **MOF-5**@DMF, **MOF-5**@MeOH, **MOF-5**@EtOH, **MOF-5**@MeCN and **MOF-5**@EtCN, as well as **MOF-D**@DMF, **MOF-D**@MeOH, **MOF-D**@EtOH, **MOF-D**@MeCN and **MOF-D**@EtCN were obtained in this way. The solvent insertion was confirmed by IR spectroscopy.

Instrumentation.

Powder XRD measurements: The samples for powder XRD measurements were mixed with a small amount of paratone oil, cut to approximately 0.3 × 0.3 × 0.3 mm^3, and placed on a sample holder mounted at 173.2 K on a Bruker APEX DUO X-ray diffractometer. Six correlated runs per sample with Phi Scan of 360 degrees and exposure times of 270 s were collected with the Cu micro-focus anode (1.54184 Å) and the CCD APEX II detector at a 150 mm distance. These runs, from −12 to −72°2θ and 6 to 36ω, were then treated and integrated with the XRW2 Eval Bruker software to produce WAXD diffraction patterns from 2.5 to 82°2θ. The patterns were treated with Diffrac.Eva version 2.0 from Bruker.

FT-Raman: The FT-Raman spectra were recorded from 0 to 4000 cm^{-1} at a 5 cm^{-1} resolution using a Bruker RFS 100/S spectrometer with the 1064 nm excitation and a light power equal to 250 mW equipped with a photomultiplier Ge-diode, cooled at liquid nitrogen temperature (77K). The peak centred between 83 and 85 cm^{-1} is considered as residual artefact from the instrument and should not be considered.

FT-IR: The IR spectra were recorded on an ABB Bomem, MB series FTIR spectrometer equipped with an ATR module from Specac at 4 cm^{-1} resolution from 600 to 4000 cm^{-1}.

Solid-state UV-vis emission and excitation spectra. These spectra were acquired either on an Edinburgh Instruments FLS980 or a Horiba PTI QM-400, both equipped with Xe lamps and single-single monochromators. Samples were either dissolved in an appropriate solvent in 10x10 mm quartz cuvettes, introduced in a glass capillary, or dispersed between quartz plates. The spectra were corrected for instrument response.

Fluorescence lifetimes. The fluorescence lifetime measurements were performed on the Edinburgh Instruments FLS980 using a microchannel plate PMT and nano-LED lasers (λ_{ex} = 395 nm; 15 mW; FWHM = 125 ns, or λ_{ex} = 443 nm; 15 mW; FWHM = 125 ns).

Measurements were performed using the time-correlated single-photon counting (TCSPC) method and data were treated by multi-exponential deconvolution analysis.

Time-resolved fluorescence spectra. The Streak camera gives a 3D image of the time resolved photoluminescence spectrum. The sample was excited by a femtosecond pulse and the emission was sent into a spectrograph to retrieve the spectral axis in *x*. The output of the spectrograph was coupled with a photocathode to generate electrons while keeping the spectral axis information. Those electrons were then accelerated in the Streak tube towards a phosphor screen while applying a time dependent transverse field ramp along the *y* axis. Thus, the electrons generated on the photocathode at different times were deflected differently on the *y* axis. By synchronizing the sweep of the ramp with the laser source and by calibrating its temporal variation, the emission kinetics were retrieved along the *y* axis. For the temporal resolution to be under 10ps, the AXIS-TRS from *Axis Photonique Inc* used a photoconductive switch (PCS) to start the tension sweep. The PCS was composed of conducting interdigitated fingers covered with a semi-conductor. By hitting the semiconductor with a laser pulse, the generated electrons allowed for the current to flow in the circuit to start the sweep on the tube. The temporal window was limited by the sweep and different electronic constrains and the repetition rate could not exceed 1 kHz. For longer temporal windows, the camera was equipped with an electronic pulse that can extend the window to 200ns with a repetition rate reaching 1MHz. The temporal resolution is limited by the inherent electronic jitter on triggering and was estimated to ~5ps.

Fast kinetic emission decay (Power-dependence) measurements. The laser source was the SHG of a Solstice (Spectra Physics) Ti-sapphire laser (λ_{ex} = 398 nm; FWHM = 75-100 ps; 0.1 mJ per pulse; rep rate = 1 kHz; spot size B500 mm). The IRF became a HWHM of ~8 ps after passing through the optics. The detector was a Streak camera (Axis-TRS, Axis Photonique Inc.) with typically less than ~8 ps resolution. The samples were dispersed between two quartz plates or introduced in a capillary. The results were globally analysed with Glotaran (https://www.glotaran.org) allowing for the extraction of a sum of independent exponentials: $I(\lambda, t) = C_1 e^{\frac{-t}{\tau_1}} + C_2 e^{\frac{-t}{\tau_2}} + C_3 e^{\frac{-t}{\tau_3}} + \cdots$

X-ray structures. **MOF-5:** A Prism-like specimen of $C_9H_0O_{10.69}Zn_{1.69}$, approximate dimensions 0.230 mm x 0.282 mm x 0.291 mm, was used for the X-ray crystallographic analysis. The X-ray intensity data were measured (λ = 0.71073 Å). The structure was solved and refined using the Bruker SHELXTL Software Package, using the space group R 3 m, with Z = 16 for the formula unit, $C_9H_0O_{10.69}Zn_{1.69}$. The final anisotropic full-matrix least-squares refinement on F^2 with 101 variables converged at R1 = 16.23%, for the observed data and wR2 = 49.18% for all data. The goodness-of-fit was 1.879. The largest peak in the final difference electron density synthesis was 3.983 $e^-/Å^3$ and the largest hole was -3.040 $e^-/Å^3$ with an RMS deviation of 0.299 $e^-/Å^3$. On the basis of the final model, the calculated density was 0.796 g/cm^3 and F(000), 3042 e^-.

$[Zn_2(BTTB)(DMF)_2•(H_2O)_3]_n$ (**MOF-D**): A yellow prism-like specimen of $C_{40}H_{46}N_2O_{13.41}Zn_2$, approximate dimensions 0.150 mm x 0.210 mm x 0.300 mm, was used for the X-ray crystallographic analysis. The X-ray intensity data were measured on a Bruker Apex DUO system equipped with a Cu Kα ImuS micro-focus source with MX optics (λ = 1.54178 Å). The structure was solved and refined using the Bruker SHELXTL Software Package, using the space group I_{mma}, with Z = 4 for the formula unit, $C_{40}H_{46}N_2O_{13.41}Zn_2$. The final anisotropic full-matrix least-squares refinement on F^2 with 150 variables converged at R1 = 11.59%, for the observed data and wR2 = 33.55% for all data. The goodness-of-fit was 1.360. The largest peak in the final difference electron density synthesis was 1.621 $e^-/Å^3$ and the largest hole was -0.722 $e^-/Å^3$ with an RMS deviation of 0.188 $e^-/Å^3$. Based on the final model, the calculated density was 0.966 g/cm^3 and F(000), 1869 e^-.

Results and Discussion

Preparation of MOFs. The identity of both MOFs was confirmed by single crystal X-ray crystallography (Table S1). Because of **MOF-5**'s sensitivity to humidity, the quality of the solid was further checked by examining the X-ray powder diffraction pattern using the original data provided in reference.[46] The homogeneity/purity of the solid phase was checked against the simulated X-ray powder diffraction pattern using the X-ray data of the single crystal with that of the experimental one (Figure S1). The presence of DMF (ν(C=O) = 1670 cm^{-1}) as well as the absence of water were confirmed by IR spectroscopy (Figure S2). The same method was used to confirm the presence of the other solvents inside both MOF's pores. It is noteworthy that the IR spectra of **MOF-5** containing water exhibits weak ν(O-H) signals.[48] Concurrently, the Raman spectra of **MOF-5** show clearly the expected signature of this MOF skeleton (Figure S2) in agreement with the literature.[49,50]

Fluorescence spectra and lifetimes. The fluorescence spectra of both MOFs (Figure 1) fall in the expected regions. For **MOF-5**@DMF, λ_{max} = 433 nm (*i.e.* in the 325-500 nm range)[29] and for $[Zn_2(BTTB)(DMF)_2 \bullet (H_2O)_3]_n$ (**MOF-D**), λ_{max} = 470 nm, which is identical to that for 3D-$[Zn_2(BTTB) \bullet (H_2O)_5]_n$ (λ_{max} ~ 470 nm).[37]

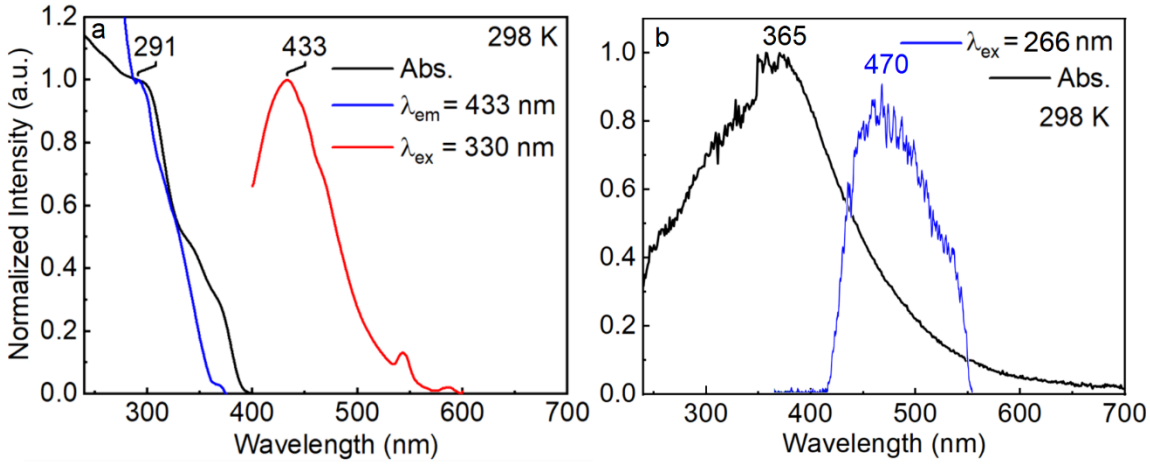

Figure 1. (a) **MOF-5**@DMF: absorption (black), excitation (blue) and fluorescence (red) spectra. (b) $[Zn_2(BTTB)(DMF)_2 \bullet (H_2O)_3]_n$ (**MOF-D**): absorption (black) and fluorescence (blue) spectra. This weaker emission spectrum was obtained using a Streak camera and a frequency tripled irradiation (λ_{exc} = 266 nm) from a Ti-sapphire laser (λ_{exc} = 798 nm).

The fluorescence lifetimes of **MOF-5**@guest were measured using TCSPC (Table 1). A representative example of fluorescence decay is provided in Figure 2. The decays are found to be biexponential, with a short component in the ps time scale and a long component in the ns time frame. The fact that the decays are biphasic is not unprecedented. Indeed, Villemot *et al*.[29] reported a double exponential decay for activated MOF (guest = air; 1.4 ± 0.1 ns and 4.5 ± 0.1 ns). The long value is relatively consistent with that obtained in this work (2.3 ± 10% at 298 K, and 4.1 ± 10% at 77 K). The same authors also demonstrated that when the water content increases from long exposure to moisture, the long component increases to 8 to 10 ns, which could be due to the presence of free H_2BDC by comparison with a neat sample. In this work, one finds that τ_{F2}(air) < τ_{F2}(DMF) < τ_{F2}(MeCN) < τ_{F2}(MeOH) at 298 K, which correlate well with the dipole moments of the liquids at room temperature (DMF > MeCN > MeOH). Concurently, τ_{F2}(air) ~ τ_{F2}(DMF) < τ_{F2}(MeCN) ~ τ_{F2}(MeOH) at 77 K. Overall, the data indicate a clear solvent dependence of this photophysical parameter, which is in line with the conclusion made by Villemot *et al*.[29] In this study, another significant and short-lived component in the 50-150 ps time scale is depicted (Figure 2) and discussed below.

Table 1. τ_F data for selected **MOF-5**@guest (TCSPC; solid state).[a]

Guest	T(K)	τ_{F1} (ps) ± 5%	τ_{F2} (ns) ± 5%
Air	298	140	2.3
	77	105	4.1
DMF	298	115	3.0
	77	54[b]	3.9
MeCN	298	140	3.6
	77	120	5.2
MeOH	298	135	4.5
	77	100	5.1

a) Note that **MOF-5**@H_2O was not investigated due to the great sensitivity of **MOF-5** towards water.[30] TCSPC measurements are time consuming and degradation might be induced from the power and duration of the excitation necessary for the measurement. b)

Not considered accurate. The FWHM of the laser pulse is 100 ps, so deconvolution does not permit accuracy below this value.

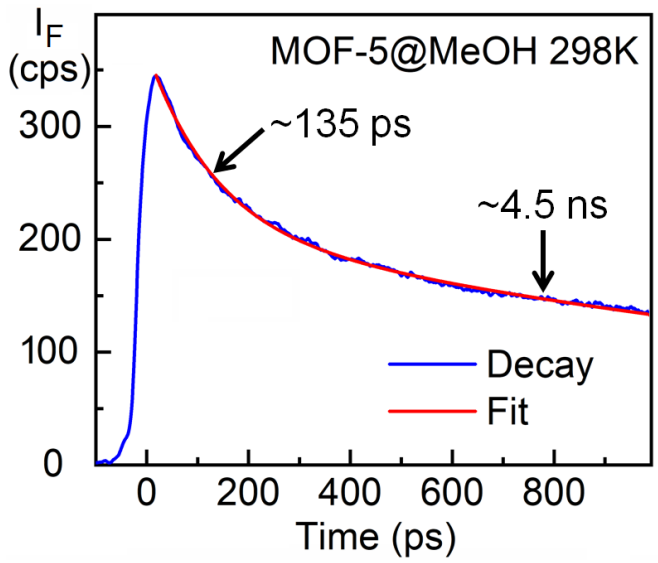

Figure 2. Fluorescence decay of **MOF-5**@MeOH (as a representative example) to stress the biphasic nature of the decay.

A Streak camera was used to extract the fluorescence lifetimes of **MOF-D**. In this case, a triple exponential was best to describe the decay curves: τ_{F1} = 0.53 ns, τ_{F2} = 2.2 ns, and τ_{F3} = 8.0 ns (uncertainties are ± 5%) at 298K. Interestingly, the τ_{F2} values increases upon lowering the temperature to 77 K, which is expected when a molecular skeleton becomes more rigid and the thermal energy decreases. Conversely, excluding uncertainties, τ_{F1} data does just the opposite. This behavior provides interesting information on the solvent-dependent mechanism, as it may reflect the increase in interactions between the guest molecule and the framework structure upon temperature decrease. Indeed, the X-ray structure at low temperature allowed to localize the water molecules inside the pores.

The proposed assignments for the shorter (*i.e.* significant component) and longer lifetimes are the different behaviors of the chromophores inside the bulk vs those nearer the surface of the MOFs. This proposal is based on the fact that the pores are filled with trapped solvent molecules, which make non-radiative deactivation pathway more likely due to chromophore-solvent collisions being more frequent, resulting in a decrease in excited state lifetimes. Moreover, upon cooling the sample to 77 K, the unit cell parameters are bound to decrease, making the trapped solvent molecules even more prone

to collisions with the chromophores, thus further reducing excited state lifetimes. Concurrently, longer lifetimes are associated with chromophores near the surface of the MOFs, which are not as tightly bound by the structure or with trapped molecules inducing collisional deactivation: excited state lifetime increases as temperatures decrease.

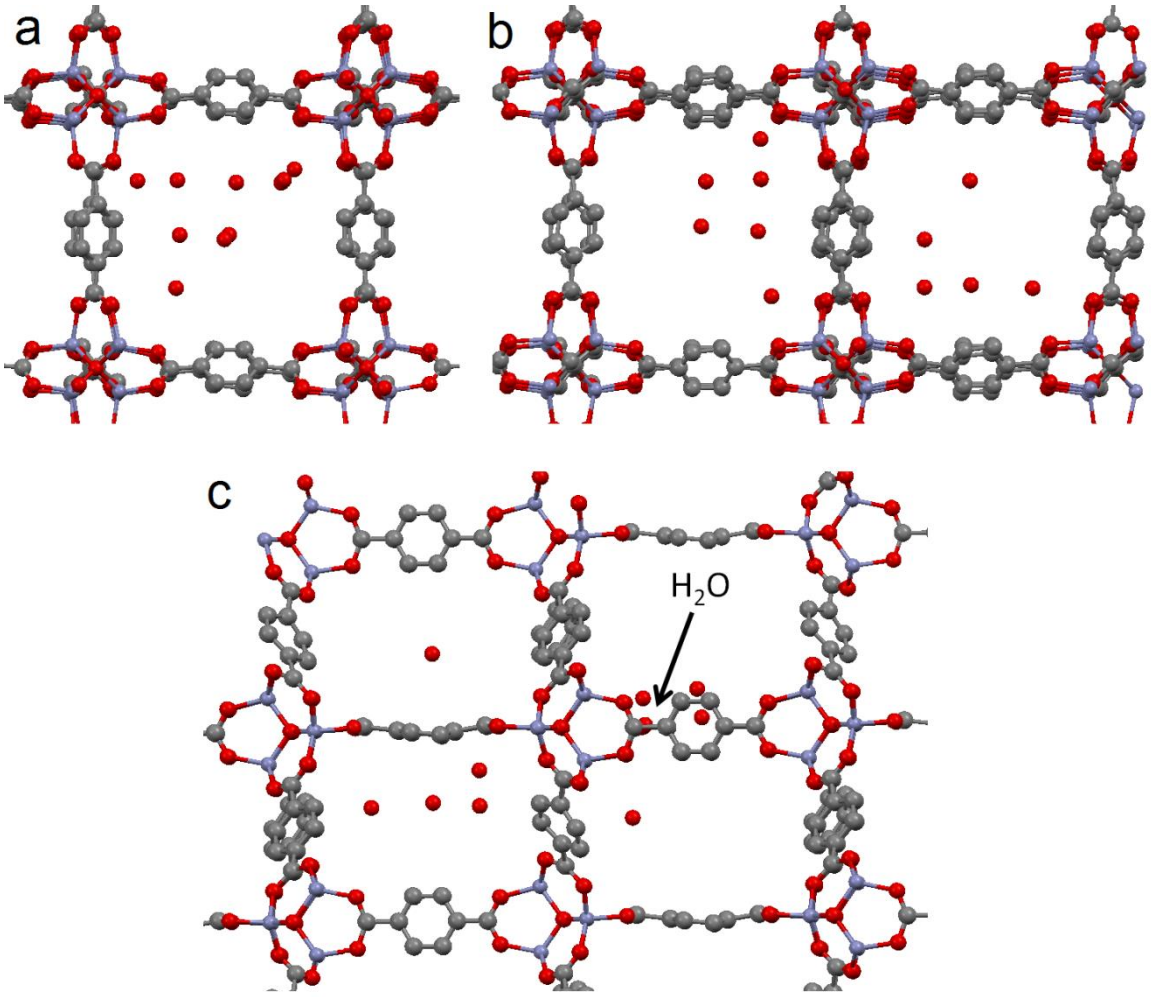

Figure 3. Ball and stick representations of the lattice of **MOF-5** at 173K in three different orientations. The closest O▪▪▪O separation (water and $-CO_2^-$) is 4.331 Å. For sake of clarity, the H-atoms and disordered C-atoms are omitted.

Crystal structures. To corroborate this proposal, the crystal structures of **MOF-5**@H_2O and **MOF-D** at 173K were solved in order to locate the solvent molecules in the lattice (Figures 3 and 4). Note that to the best of our knowledge, this quest was never performed

before on **MOF-5**, and that **MOF-5**@H_2O was selected to make suitable comparisons with **MOF-D**, which contains three water molecules in the unit cell.

For **MOF-5**, three different orientations are presented and partial electronic density associated with the water molecules has been localized. This disorder is most likely to be due to static disorder at this temperature. More importantly, one notes that these density spots are well located in the center of the pores thus indicating no preference or no strong interaction between the water molecules and the O-atoms of the carboxylate groups. Indeed, the closest O▪▪▪O separation between water and -CO_2^-, is 4.331 Å, well within realistic ranges of strong static H-bonds.

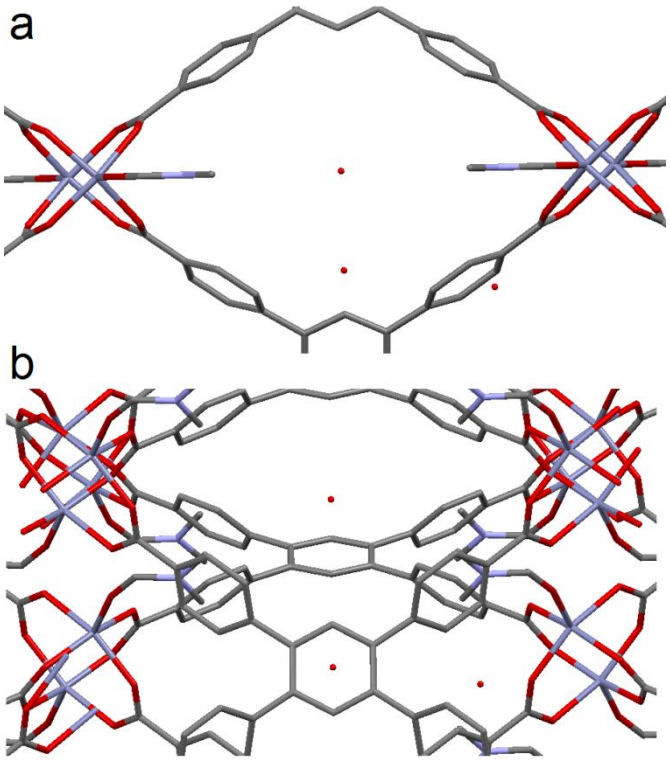

Figure 4. Stick representations of the lattice of **MOF-D** at 173K in two different orientations. The red dots are the O-atoms of the water molecules and the closest O▪▪▪O separation (water and -CO_2^-) is 3.897 Å. For sake of clarity, the H-atoms are not shown.

Similarly, two orientations of the crystal lattice of **MOF-D** at 173 K are presented in Figure 4 and the same observation can be made. The closest O▪▪▪O separation (water and -CO_2^-) is 3.897 Å. Part of the explanation may stem from the presence of *ortho*-H atoms in the plane of the benzene-CO_2^- units exhibiting some steric hindrance. In conclusion,

the BDC and BTTB chromophores are surrounded by solvent molecules in a similar manner as they would be in solution, except that solvent molecules are clearly confined inside the pores.

Power dependence of the fluorescence intensity. Time-resolved fluorescence spectra measurements were performed upon increasing the excitation flux. Plots reporting the highest absolute emission intensity during each decay against excitation power allow for the visualization of 1) the linearity or non-linearity of the response, indicating whether a proportional number of photons are emitted relative to the number of absorbed photons, and 2) the comparison of the fluorescence intensity influenced by the guest molecule. Both MOFs at high (298 K) and low (77 K) temperatures exhibit a quasi-linear behavior when plotted against linear laser power (Figure 3). This linearity is indicative that no singlet-singlet annihilation occurs ($S_1 + S_1 \rightarrow S_n + S_0$ + heat) meaning that excitons are not very mobile across the framework in both MOFs.

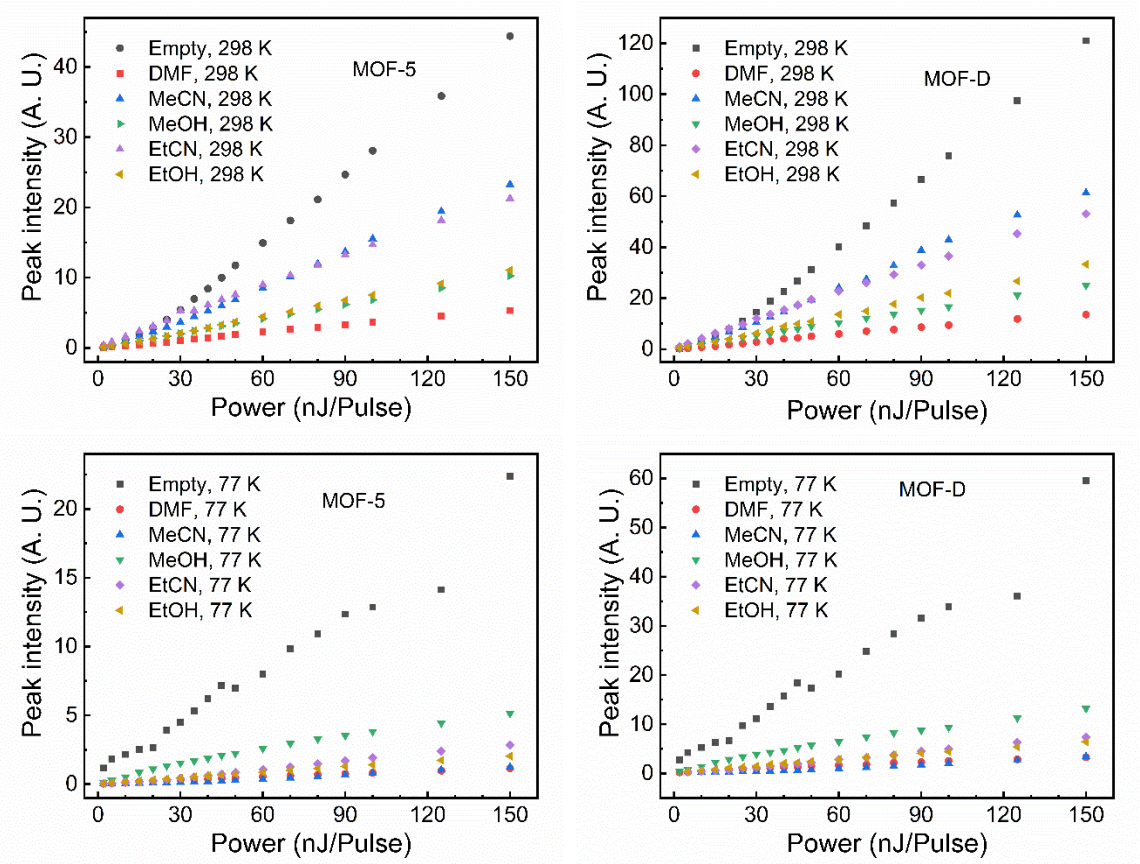

Figure 5: Peak emission intensities of **MOF-5** (left) and **MOF-D** (right) at 298K (top) and 77K (bottom), with different guests inside the pores.

The presence of a guest has an important influence, as both MOFs give off the strongest emission when “empty” (filled with air). When a solvent is present, a very strong trend emerges; both nitriles cut the emissive intensity by roughly half, both alcohols reduce it by roughly ¾, and DMF results in the most drastic intensity decrease of roughly 90% compared to the empty MOF luminescence. At 77 K trends are not as stark, but the presence of solvent solvents still reduces the emissive intensity by factors of 3-10. It is noteworthy that MeOH seems is the guest which decreases the absolute fluorescence intensity the least for both MOFs. This “bunched-up” behavior of all solvents may be explained by the fact that, at low temperature, molecules cannot move around in the MOF’s cavities. In this case, the presence of a solvent (*i.e*. “*something* denser than air is inside the pores”) may be as important as the nature of the molecule ("*what* is there”).

When analyzing the influence of temperature, one notes that all emission intensities tend to decrease with the temperature. Empty MOFs see their fluorescence intensity cut by roughly half. Nitriles exhibit the largest relative decrease of fluorescence intensity when cooled form 298K to 77K, whereas alcohols and DMF see moderate decreases. The observation is in line with the decrease in fluorescence lifetimes upon cooling at 77K observed in Table 1. Indeed, with $k_F = \Phi_F/\tau_F$ if τ_F decreases, then Φ_F (fluorescence quantum yield) should decrease proportionally, and consequently with $k_{nr} = (1-\Phi_F)/\tau_F$, the non-radiative rate constant increases. Both series of MOF@MeOHs and MOFs@air exhibit the least decrease in fluorescence intensity, again demonstrating that the nature of guest molecules has a significant impact on their emission properties.

Excitation energy migration. Despite the rich photocatalytic properties of **MOF-5**,[2,3,12–21,4,22–25,5–11] it is quite surprising that no S_1-S_1 annihilation occurs. This result indicates that there no noticeable excitation energy migration across both **MOF-5**’s and **MOF-D**’s scaffolding. To explain this observation, one has to refer to the Förster (often called Fluorescence Resonance Energy Transfer: FRET) and Dexter theories for energy transfer. The rate of energy transfer, k_{ET}, operating according a FRET mechanism is given by eq. 1:[51]

$$k_{ET} = \frac{\Phi_F^o(D)}{\tau_F^o(D)} \frac{k^2}{r^6} \left(\frac{9000\,(\ln 10)}{128\,\pi^5 n^4 N_a} \right) \frac{\int F_D(\lambda)\varepsilon_A(\lambda)\lambda^4\,d\lambda}{\int F_D(\lambda)\,d\lambda} \qquad (1)$$

where the terms $\Phi_F°(D)$, $\tau_F°(D)$, κ^2, r^6, n, N_a, F_D, ε_A and λ are respectively the fluorescence quantum yield and lifetime ($k_F^o = \Phi_F°(D)/\tau_F°(D)$, the radiative rate constant) of the donor in the absence of an energy acceptor, the orientation factor linked to the transition moments of the donor and acceptor ($0 < \kappa^2 < 4$), the center-to-center separation between the donor and acceptor units, the refractive index, the Avogadro's number, the intensity of the donor fluorescence and the absorptivity of the acceptor, and the wavelength. Concurrently, k_{ET} operating through a double electron exchange (Dexter mechanism) is given by eq. 2:[52]

$$k_{ET} = \frac{K}{\hbar} e^{\frac{-2R}{L}} \frac{\int F_D(\lambda)\varepsilon_A(\lambda)\lambda^4 \, d\lambda}{\int F_D(\lambda) \, d\lambda} \quad (2)$$

$$J = \frac{\int F_D(\lambda)\varepsilon_A(\lambda)\lambda^4 \, d\lambda}{\int F_D(\lambda) \, d\lambda} \quad (3)$$

where ***R***, ***K***, and ***L*** are respectively the center-to-center separation between the donor and acceptor units, an experimental constant, and the average Bohr radius. In brief, when ε_A is small, ***J*** (spectral overlap integral, eq. 3) is small, and k_{ET} becomes negligible.

For the BDC and BTTB ligands, the ε values are not known in the solid state since the Beer-Lambert law does not apply and that the baseline is not corrected for light scattering. Instead, the ε values have been evaluated in solution using the corresponding acids (data placed in the SI). For H_2BDC, ε ~ 3 $M^{-1}cm^{-1}$ at 390 nm (where the absorption and fluorescence curves cross and therefore being the highest point in the ***J*** spectral overlap integral, eq. 3), which is negligible. For example, porphyrin-based MOFs have a strong tendency to promote ultrafast exciton energy migrations,[53–63] which is consistent with large ε values in its lowest energy Q-bands (in the order of 10^4 $M^{-1}cm^{-1}$) and consequently their large ***J*** integrals.[64] Concurrently, H_4BTTB exhibits an ε value of ~ 327 $M^{-1}cm^{-1}$ at 410 nm, which is also not very large. In conclusion, the absence of excitation energy migration in **MOF-5** and **MOF-D** is simply due to unfavorable ***J*** integrals, thus rendering k_{ET} very slow (i.e. unimolecular deactivation occurs faster).

Conclusion

The results obtained in this study corroborate those obtained by previous investigation:[29] photophysical properties of MOFs can be strongly influenced by the nature of guest

molecules and can be correlated with the dipole moments in the case of liquids (DMF, MeCN and MeOH). This study also highlights near-inexistent exciton hopping across the structures of **MOF-5** and **MOF-D**. A closer look at why this is so, the main reason stems from a very small values of ε, which renders the *J* overlap integrals of the Forster and Dexter theories small, not to say negligible. This outcome (*i.e*. no or very low number of exciton hopping across the networks) indicates that the rich photocatalytic activity mentioned above[2,3,12–21,4,22–25,5–11] is not aided by the excitation energy migration. Therefore, the interior of the particles or nanoparticles does not contribute by the so-called antenna effect to the photochemical transformations that may occur at the surface of these porous objects. This conclusion is quite important for the design of efficient MOF-based photocatalysts.

Acknowledgments

This work was supported by the Natural Sciences and Engineering Research Council of Canada (NSERC/CRSNG). P.A. thanks *Université de Sherbrooke* for the *Bourse d'Excellence Hydro-Québec* doctoral scholarship grant.

AUTHOR INFORMATION

Corresponding Author

*E-mail: Pierre.Harvey@USherbrooke.ca (P.D.H.)

Author Contributions

Synthesis of ligands and MOFs (AS and PA); characterization of MOFs (AS, PA, PLK and DF); data treatment and figure creation (AS, PA, PDH and PLK); writing -original draft (PDH and AS); writing -review and proofreading (PDH, AS and PA); supervision, project administration, funding acquisition (PDH). All authors have read and agreed to the published version of the manuscript.

Notes

The authors declare no competing financial interest.

Supporting information containing further characterization data as described in the text is available free of charge.

References

1 O. V. Kharissova, B. I. Kharisov, I. E. Ulyand and T. H. García, Catalysis using metal–organic framework-derived nanocarbons: Recent trends, *J. Mater. Res.*, 2020, **35**, 2190–2207.

2 Y. Xiao, X.-L. Wang, H. Yu, Y. Yang and X. Dong, MOF-5 derived C-doped ZnO decorated with Cu cocatalyst for enhancing visible-light driven photocatalytic hydrogen evolution, *J. Phys. Chem. Solids*, 2021, **149**, 109793.

3 L. Cui, X. Zou, Y. Liu, X. Li, L. Jiang, C. Li, L. Yang, M. Yu and Y. Wang, Dramatic enhancement of photocatalytic H2 evolution over hydrolyzed MOF-5 coupled Zn0.2Cd0.8S heterojunction, *J. Colloid Interface Sci.*, 2020, **577**, 233–241.

4 H.-X. Liu, T.-T. Liu, T. Huang, Z.-B. Fang, L. Li, Q. Yin, R. Cao, X.-Q. Gong and T.-F. Liu, Trace of molecular doping in metal–organic frameworks: drastic change in the electronic band structure with a preserved topology and porosity, *J. Mater. Chem. A*, 2020, **8**, 12370–12377.

5 X. Hao, Z. Cui, J. Zhou, Y. Wang, Y. Hu, Y. Wang and Z. Zou, Architecture of high efficient zinc vacancy mediated Z-scheme photocatalyst from metal-organic frameworks, *Nano Energy*, 2018, **52**, 105–116.

6 W. Zhen, J. Ma and G. Lu, Small-sized Ni(1 1 1) particles in metal-organic frameworks with low over-potential for visible photocatalytic hydrogen generation, *Appl. Catal. B Environ.*, 2016, **190**, 12–25.

7 S. Xiao, P. Liu, W. Zhu, G. Li, D. Zhang and H. Li, Copper Nanowires: A Substitute for Noble Metals to Enhance Photocatalytic H 2 Generation, *Nano Lett.*, 2015, **15**, 4853–4858.

8 X. Zhao, J. Feng, J. Liu, J. Lu, W. Shi, G. Yang, G. Wang, P. Feng and P. Cheng, Metal–Organic Framework-Derived ZnO/ZnS Heteronanostructures for Efficient Visible-Light-Driven Photocatalytic Hydrogen Production, *Adv. Sci.*, 2018, **5**, 1700590.

9 M. Z. Hussain, G. S. Pawar, Z. Huang, A. A. Tahir, R. A. Fischer, Y. Zhu and Y. Xia, Porous ZnO/Carbon nanocomposites derived from metal organic frameworks for highly efficient photocatalytic applications: A correlational study, *Carbon N. Y.*, 2019, **146**, 348–363.

10 Q. V. Thi, M. S. Tamboli, Q. Thanh Hoai Ta, G. B. Kolekar and D. Sohn, A nanostructured MOF/reduced graphene oxide hybrid for enhanced photocatalytic efficiency under solar light, *Mater. Sci. Eng. B*, 2020, **261**, 114678.

11 Y.-Y. Tong, Y.-F. Li, L. Sun, R. Yang, S. Zhang, Y. Fu, L. Cao and R. Chen, The prominent photocatalytic activity with the charge transfer in the organic ligand for [Zn4O(BDC)3] MOF-5 decorated Ag3PO4 hybrids, *Sep. Purif. Technol.*, 2020, **250**, 117142.

12 A. Chakraborty and H. Acharya, ZnAl–LDH/MOF-5 heterostructure nanocomposite for photocatalytic degradation of organic dyes under sunlight irradiation, *New J. Chem.*, 2023, **47**, 1498–1507.

13 B. Sarwar, A. Khan, T. Fazal, M. Aslam, N. Qaisrani and A. Ahmed, Synthesis of Novel MOF-5 Based BiCoO3 Photocatalyst for the Treatment of Textile Wastewater, *Sustainability*, 2022, **14**, 12885.
14 Y. Yang, Z. Xing, W. Kong, C. Wu, H. Peng, Z. Li and W. Zhou, Metal–organic framework (MOF)-5/CuO@ZnIn 2 S 4 core–shell Z-scheme tandem heterojunctions for improved charge separation and enhanced photocatalytic performance, *Nanoscale*, 2022, **14**, 14741–14749.
15 T. Yao, Y. Tan, Y. Zhou, Y. Chen and M. Xiang, Preparation of core-shell MOF-5/Bi2WO6 composite for the enhanced photocatalytic degradation of pollutants, *J. Solid State Chem.*, 2022, **308**, 122882.
16 A. Chen, J. Zhang, Y. Zhou and H. Tang, Preparation of a zinc-based metal–organic framework (MOF-5)/BiOBr heterojunction for photodegradation of Rhodamine B, *React. Kinet. Mech. Catal.*, 2021, **134**, 1003–1015.
17 S. A. Younis, P. Serp and H. N. Nassar, Photocatalytic and biocidal activities of ZnTiO2 oxynitride heterojunction with MOF-5 and g-C3N4: A case study for textile wastewater treatment under direct sunlight, *J. Hazard. Mater.*, 2021, **410**, 124562.
18 A. Jabbar, M. Fiaz, S. Rani, M. N. Ashiq and M. Athar, Incorporation of CuO/TiO2 Nanocomposite into MOF-5 for Enhanced Oxygen Evolution Reaction (OER) and Photodegradation of Organic Dyes, *J. Inorg. Organomet. Polym. Mater.*, 2020, **30**, 4043–4052.
19 Y.-Y. Tong, Y.-F. Li, L. Sun, R. Yang, S. Zhang, Y. Fu, L. Cao and R. Chen, The prominent photocatalytic activity with the charge transfer in the organic ligand for [Zn4O(BDC)3] MOF-5 decorated Ag3PO4 hybrids, *Sep. Purif. Technol.*, 2020, **250**, 117142.
20 M. Zebardast, A. F. Shojaei and K. Tabatabaeian, Enhanced removal of methylene blue dye by bimetallic nano-sized MOF-5s, *Iran. J. Catal.*, 2018, **8**, 297–309.
21 M. Naimi Joubani, M. A. Zanjanchi and S. Sohrabnezhad, A novel Ag/Ag 3 PO 4 - IRMOF-1 nanocomposite for antibacterial application in the dark and under visible light irradiation, *Appl. Organomet. Chem.*, , DOI:10.1002/aoc.5575.
22 S. R. Thakare and S. M. Ramteke, Fast and regenerative photocatalyst material for the disinfection of E. coli from water: Silver nano particle anchor on MOF-5, *Catal. Commun.*, 2017, **102**, 21–25.
23 G. Fan, J. Zhou, X. Zheng, J. Luo, L. Hong and F. Qu, Fast photocatalytic inactivation of Microcystis aeruginosa by metal-organic frameworks under visible light, *Chemosphere*, 2020, **239**, 124721.
24 X. Qin, T. Qiang, L. Chen and S. Wang, Construction of 3D N-CQD/MOF-5 photocatalyst to improve the photocatalytic performance of MOF-5 by changing the electron transfer path, *Microporous Mesoporous Mater.*, 2021, **315**, 110889.
25 L. Su, Y. Zhang, X. Qiu, J. Han and Z. Tang, Photocatalytic Carboxylation of Phenyl Halides with CO2 by Metal-Organic Frameworks Materials, *Chinese J. Chem.*, 2021, **39**, 312–316.
26 J. He, K.-K. Yee, Z. Xu, M. Zeller, A. D. Hunter, S. S.-Y. Chui and C.-M. Che, Thioether Side Chains Improve the Stability, Fluorescence, and Metal Uptake of a Metal–Organic Framework, *Chem. Mater.*, 2011, **23**, 2940–2947.
27 S. Xu, L. Zhan, C. Hong, X. Chen, X. Chen and M. Oyama, Metal–organic

framework-5 as a novel phosphorescent probe for the highly selective and sensitive detection of Pb(II) in mussels, *Sensors Actuators B Chem.*, 2020, **308**, 127733.
28 P. Kumar, A. K. Paul and A. Deep, Sensitive chemosensing of nitro group containing organophosphate pesticides with MOF-5, *Microporous Mesoporous Mater.*, 2014, **195**, 60–66.
29 V. Villemot, M. Hamel, R. B. Pansu, I. Leray and G. H. V. Bertrand, Unravelling the true MOF-5 luminescence, *RSC Adv.*, 2020, **10**, 18418–18422.
30 N. A. Rodríguez, R. Parra and M. A. Grela, Structural characterization, optical properties and photocatalytic activity of MOF-5 and its hydrolysis products: implications on their excitation mechanism, *RSC Adv.*, 2015, **5**, 73112–73118.
31 M. Ji, X. Lan, Z. Han, C. Hao and J. Qiu, Luminescent Properties of Metal–Organic Framework MOF-5: Relativistic Time-Dependent Density Functional Theory Investigations, *Inorg. Chem.*, 2012, **51**, 12389–12394.
32 T. Lee, Z. X. Liu and H. L. Lee, A Biomimetic Nose by Microcrystals and Oriented Films of Luminescent Porous Metal–Organic Frameworks, *Cryst. Growth Des.*, 2011, **11**, 4146–4154.
33 S. Bordiga, C. Lamberti, G. Ricchiardi, L. Regli, F. Bonino, A. Damin, K.-P. Lillerud, M. Bjorgen and A. Zecchina, Electronic and vibrational properties of a MOF-5 metal–organic framework: ZnO quantum dot behaviour, *Chem. Commun.*, 2004, 2300–2301.
34 X. Yang and D. Yan, Long-afterglow metal–organic frameworks: reversible guest-induced phosphorescence tunability, *Chem. Sci.*, 2016, **7**, 4519–4526.
35 P. L. Feng, J. J. Perry, S. Nikodemski, B. W. Jacobs, S. T. Meek and M. D. Allendorf, Assessing the Purity of Metal−Organic Frameworks Using Photoluminescence: MOF-5, ZnO Quantum Dots, and Framework Decomposition, *J. Am. Chem. Soc.*, 2010, **132**, 15487–15489.
36 F. Tian, X. Zhang and Y. Chen, Fabrication and Photoluminescence Property of ZnO Nanoparticle/Metal–Organic Framework Hybrid Material, *Chem. Lett.*, 2016, **45**, 388–390.
37 W. Cheng, T. Wang, W. Xu, Y. Zhang, J. Zhang and M. Fang, Syntheses of new topology BTTB-based metal–organic frameworks in CH3CN/H2O mixed solvents, *J. Coord. Chem.*, 2016, **69**, 2220–2230.
38 S. Sanda, S. Parshamoni, S. Biswas and S. Konar, Highly selective detection of palladium and picric acid by a luminescent MOF: a dual functional fluorescent sensor, *Chem. Commun.*, 2015, **51**, 6576–6579.
39 S. M. Pratik and C. J. Cramer, Predicted Efficient Visible-Light Driven Water Splitting and Carbon Dioxide Reduction Using Photoredox-Active UiO-NDI Metal Organic Framework, *J. Phys. Chem. C*, 2019, **123**, 19778–19785.
40 S. Choi, W.-J. Jung, K. Park, S.-Y. Kim, J.-O. Baeg, C. H. Kim, H.-J. Son, C. Pac and S. O. Kang, Rapid Exciton Migration and Amplified Funneling Effects of Multi-Porphyrin Arrays in a Re(I)/Porphyrinic MOF Hybrid for Photocatalytic CO2 Reduction, *ACS Appl. Mater. Interfaces*, 2021, **13**, 2710–2722.
41 P. Asselin and P. D. Harvey, Visible-Light-Driven Production of Solar Fuels Catalyzed by Nanosized Porphyrin-Based Metal–Organic Frameworks and Covalent–Organic Frameworks: A Review, *ACS Appl. Nano Mater.*, 2022, **5**,

6055–6082.
42 H. Zhang, J. Wei, J. Dong, G. Liu, L. Shi, P. An, G. Zhao, J. Kong, X. Wang, X. Meng, J. Zhang and J. Ye, Efficient Visible-Light-Driven Carbon Dioxide Reduction by a Single-Atom Implanted Metal-Organic Framework, *Angew. Chemie*, 2016, **128**, 14522–14526.
43 L. Cao, Z. Lin, W. Shi, Z. Wang, C. Zhang, X. Hu, C. Wang and W. Lin, Exciton Migration and Amplified Quenching on Two-Dimensional Metal–Organic Layers, *J. Am. Chem. Soc.*, 2017, **139**, 7020–7029.
44 P. Asselin, A. Schlachter, D. Fortin, P.-L. Karsenti and P. D. Harvey, Structural Influence on Exciton Migration and Singlet Oxygen Photosensitization in Porphyrinic Metal–Organic Coordination Networks, *Chem. Mater.*, 2022, **34**, 7242–7255.
45 O. K. Farha, K. L. Mulfort and J. T. Hupp, An Example of Node-Based Postassembly Elaboration of a Hydrogen-Sorbing, Metal−Organic Framework Material, *Inorg. Chem.*, 2008, **47**, 10223–10225.
46 H. Li, M. Eddaoudi, M. O'Keeffe and O. M. Yaghi, Design and synthesis of an exceptionally stable and highly porous metal-organic framework, *Nature*, 1999, **402**, 276–279.
47 S. Hausdorf, F. Baitalow, T. Böhle, D. Rafaja and F. O. R. L. Mertens, Main-Group and Transition-Element IRMOF Homologues, *J. Am. Chem. Soc.*, 2010, **132**, 10978–10981.
48 T. Tachikawa, J. R. Choi, M. Fujitsuka and T. Majima, Photoinduced Charge-Transfer Processes on MOF-5 Nanoparticles: Elucidating Differences between Metal-Organic Frameworks and Semiconductor Metal Oxides, *J. Phys. Chem. C*, 2008, **112**, 14090–14101.
49 R. A. Rather and Z. N. Siddiqui, Silver phosphate supported on metal–organic framework (Ag3PO4 @MOF-5) as a novel heterogeneous catalyst for green synthesis of indenoquinolinediones, *Appl. Organomet. Chem.*, , DOI:10.1002/aoc.5176.
50 M. Fiaz, M. Kashif, M. Fatima, S. R. Batool, M. A. Asghar, M. Shakeel and M. Athar, Synthesis of Efficient TMS@MOF-5 Catalysts for Oxygen Evolution Reaction, *Catal. Letters*, 2020, **150**, 2648–2659.
51 T. Förster, Energiewanderung und Fluoreszenz, *Naturwissenschaften*, 1946, **33**, 166–175.
52 D. L. Dexter, A Theory of Sensitized Luminescence in Solids, *J. Chem. Phys.*, 1953, **21**, 836–850.
53 P. M. Stanley, K. Hemmer, M. Hegelmann, A. Schulz, M. Park, M. Elsner, M. Cokoja and J. Warnan, Topology- and wavelength-governed CO2 reduction photocatalysis in molecular catalyst-metal–organic framework assemblies, *Chem. Sci.*, 2022, **13**, 12164–12174.
54 H.-J. Son, C. Pac and S. O. Kang, Inorganometallic Photocatalyst for CO2 Reduction, *Acc. Chem. Res.*, 2021, **54**, 4530–4544.
55 S. Patwardhan, S. Jin, H.-J. Son and G. C. Schatz, Ultrafast Energy Migration in Porphyrin-based Metal Organic Frameworks (MOFs), *MRS Proc.*, 2013, **1539**, mrss13-1539-d06-06.
56 S. M. Shaikh, S. Ilic, B. J. Gibbons, X. Yang, E. Jakubikova and A. J. Morris, Role

of a 3D Structure in Energy Transfer in Mixed-Ligand Metal–Organic Frameworks, *J. Phys. Chem. C*, 2021, **125**, 22998–23010.

57 S. Choi, W.-J. Jung, K. Park, S.-Y. Kim, J.-O. Baeg, C. H. Kim, H.-J. Son, C. Pac and S. O. Kang, Rapid Exciton Migration and Amplified Funneling Effects of Multi-Porphyrin Arrays in a Re(I)/Porphyrinic MOF Hybrid for Photocatalytic CO2 Reduction, *ACS Appl. Mater. Interfaces*, 2021, **13**, 2710–2722.

58 C. Gu, H. Zhang, J. Yu, Q. Shen, G. Luo, X. Chen, P. Xue, Z. Wang and J. Hu, Assembled Exciton Dynamics in Porphyrin Metal–Organic Framework Nanofilms, *Nano Lett.*, 2021, **21**, 1102–1107.

59 X. Li, J. Yu, D. J. Gosztola, H. C. Fry and P. Deria, Wavelength-Dependent Energy and Charge Transfer in MOF: A Step toward Artificial Porous Light-Harvesting System, *J. Am. Chem. Soc.*, 2019, **141**, 16849–16857.

60 M. Adams, M. Kozlowska, N. Baroni, M. Oldenburg, R. Ma, D. Busko, A. Turshatov, G. Emandi, M. O. Senge, R. Haldar, C. Wöll, G. U. Nienhaus, B. S. Richards and I. A. Howard, Highly Efficient One-Dimensional Triplet Exciton Transport in a Palladium–Porphyrin-Based Surface-Anchored Metal–Organic Framework, *ACS Appl. Mater. Interfaces*, 2019, **11**, 15688–15697.

61 S. M. Shaikh, A. Chakraborty, J. Alatis, M. Cai, E. Danilov and A. J. Morris, Light harvesting and energy transfer in a porphyrin-based metal organic framework, *Faraday Discuss.*, 2019, **216**, 174–190.

62 S. Goswami, M. Chen, M. R. Wasielewski, O. K. Farha and J. T. Hupp, Boosting Transport Distances for Molecular Excitons within Photoexcited Metal–Organic Framework Films, *ACS Appl. Mater. Interfaces*, 2018, **10**, 34409–34417.

63 S. Goswami, L. Ma, A. B. F. Martinson, M. R. Wasielewski, O. K. Farha and J. T. Hupp, Toward Metal–Organic Framework-Based Solar Cells: Enhancing Directional Exciton Transport by Collapsing Three-Dimensional Film Structures, *ACS Appl. Mater. Interfaces*, 2016, **8**, 30863–30870.

64 A. Langlois and P. D. Harvey, Maple^{TM}-assisted calculations of the J-integral: a key parameter for the understanding of excited state energy transfer in porphyrins and other chromophores, *J. Porphyr. Phthalocyanines*, 2014, **18**, 666–674.

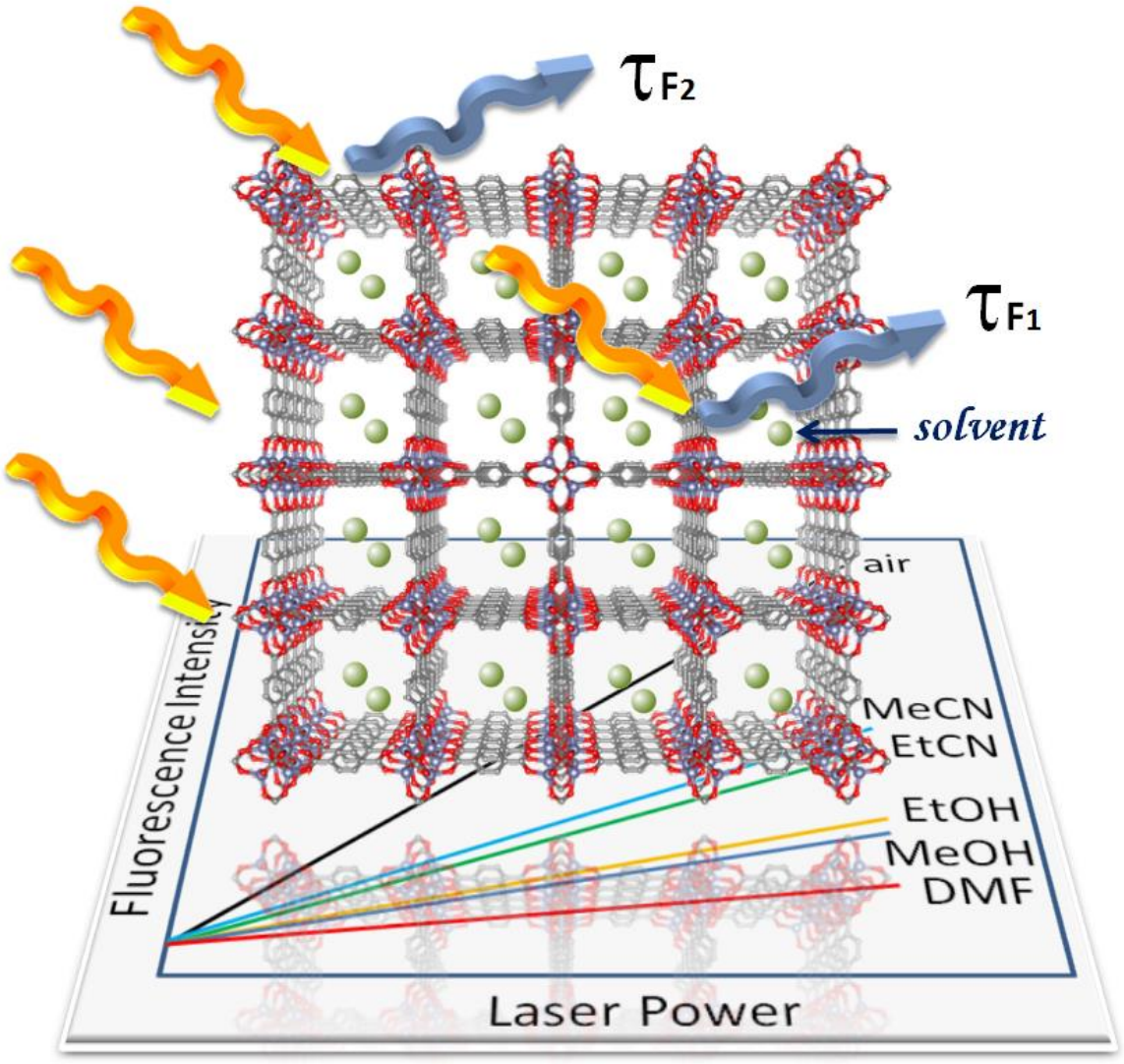
τF2
τF1
solvent
air
MeCN
EtCN
EtOH
MeOH
DMF
Fluorescence Intensity
Laser Power

TOC art